Volume 1 | Number 1 | Jan 2013 | Pages 1–100

Journal of
Materials Chemistry C

Materials for optical and electronic devices
www.rsc.org/materialsC

ROYAL SOCIETY
OF CHEMISTRY

ROYAL SOCIETY
OF CHEMISTRY

www.rsc.org/materialsC

Journal of Materials Chemistry C

PAPER

High thermoelectric performance in Tellurium doped Paracostibite

R. Chmielowski[a*†], S. Bhattacharya[b†], W. Xie[c], D. Péré[a], S. Jacob[a], R. Stern[b], K. Moriya[a], A. Weidenkaff[c], G. K. H. Madsen[b] and G. Dennler[a]

Paracostibite (CoSbS) has recently been identified as a promising thermoelectric (TE) material, yet its full potential remains to be attained. We present herein an integrated method based on high throughput DFT computations validated with experiments that has allowed us to identify Tellurium on Antimony site as a much more effective dopant than formerly used Nickel on Cobalt site. By carrying out a systematic adjustment optimization of the experimental parameters, we achieve a power factor as high as 2.7 mW.m^{-1}.K^{-2} at 543K which is maintained up to 730 K. This is, to the best of our knowledge, the largest value reported on polycrystalline metal sulfides.

Introduction

Thermoelectric generators (TEGs) have applications in direct power generation as well as in domestic, transportation and industrial waste heat recovery sectors. However, large scale utilization of the thermoelectric effect as a renewable energy resource will eventually depend on the cost, the availability, the toxicity and the overall performance of the active materials used in the TEGs.[1-3] Metal sulfide compounds and natural occurring minerals have recently been attracting a considerable attention as thermoelectrics because they fulfil the requirements for large scale deployment.[4] The performance of a thermoelectric material is characterized by its figure-of-merit $zT = (S^2.\sigma/\kappa)T$, where S, σ, κ and T are Seebeck coefficient, electrical conductivity, thermal conductivity and temperature, respectively. Designing better performing thermoelectric materials is an arduous task because one needs to simultaneously tune S, σ and κ. As these transport quantities are interdependent, the experimental optimization of the zT value of a given material can take several years, like it was the case for the now commercially available Bi$_2$Te$_3$. In order to accelerate the discovery and the

optimization of new thermoelectric materials, we have decided to focus our effort upon the power factor (PF) defined by PF = $S^2.\sigma$.[5] The most important advantage of this approach is that the PF of a material strongly depends on its electronic structure and is mainly governed by intrinsic characteristics of the material. This descriptor is thus well suited for a computational approach. In the present paper, we show how the combined band structure calculations and high-throughput screening of external carrier controlling defects can support the experimental optimization of a new thermoelectric material, namely CoSbS. Besides, we report that this multidisciplinary approach allowed us to reach with this very material power factors as high as 2.7 mW.m^{-1}.K^{-2}. To the best of our knowledge, such a high power factor has never been reported on polycrystalline semiconducting metal sulfides.

Recently, sulfur based polycrystalline materials such as tetrahedrite,[6-8] lead sulfide,[9-11] copper sulfides,[4,12] tin sulfide,[5,13] shandite,[14] titanium sulfide[15] and bismuth sulfide,[16,17] have been investigated as promising thermoelectrics. Among them, PbS and Cu$_2$S appeared as the ones showing the best performances. The power factor of PbS has been reported to reach values as high as 1.2 mW.m^{-1}.K^{-2} and its zT has been measured above 1 in both p-type and n-type materials.[10,11] However, the fact that this material comprises Pb may prevent its large deployment because of the Restriction of the Use of Certain Hazardous Substances (RoHS). In the case of Cu$_{2-x}$S, PFs between 0.8 and 1.0 mW.m^{-1}.K^{-2} and a zT between 0.5 to 1.6 (between 600 and 1000K) have been reported by several groups.[4,12] Unfortunately, this material is prone to significant Cu^{2+} ion migration, what prohibits its usage in functional TEGs.[18] Paracostibite (CoSbS), one of the two cobalt antimony sulfides known from mineralogy has been

a. IMRA Europe S.A.S., 220 rue Albert Caquot, BP 2013, 06904 Sophia Antipolis, France. *E-mail : chmielowski@imra-europe.com
b. CMAT, ICAMS, Ruhr-Universität Bochum, Germany.
c. Institute of Materials Science, University of Stuttgart, Heisenbergstraße 3, Stuttgart, Germany.

recently reported to possess an attractive thermoelectric potential. Unlike its Costibite counterpart, Paracostibite is calculated by Density Functional Theory (DFT) to be stable and to lie on the corresponding elemental convex-hull. The unit cell parameters of the Paracostibite are a = 584.2(3), b = 595.1(3), c = 1166.6(4) pm with Pbca (no. 61) space group.[19][19] Note that Paracostibite is hereafter referred by its chemical formula, CoSbS. The structure and valence electron count in CoSbS is similar to the orthorhombic marcasite FeS_2 compound. The CoSbS orthorhombic cell illustrated in Figure S1 is isoelectronic and isostructural with respect to the FeS_2 marcasite structure. Here Co replaces Fe and Sb replaces one of the S atoms.

CoSbS is known to be a semiconducting material with an experimentally defined band gap of around 0.5 eV.[20] The first experimental work focusing on the thermoelectric properties of CoSbS demonstrated a Seebeck coefficient around 200 µV.K^{-1}.[21] Thereafter, D. Parker et al.[22] and very recently Z. Liu et al.[23] have shown that a power factor of 1.6 mW.m^{-1}.K^{-2} at 723K and 2.0 mW.m^{-1}.K^{-2} at 873K, respectively, can be achieved when CoSbS is n-doped by partially substituting Co with Ni. The goal of our study is thus to assess, in an efficient manner guided by computational high-throughput defect thermochemistry, whether better dopants could be identified in order to reach a higher density of charge carriers, and thereby improved thermoelectric performances.

Methods

Pure and doped CoSbS samples were prepared from high purity elements reacted in evacuated Quartz Ampoules (QA) followed by Spark Plasma Sintering (SPS). The raw powders were Co, Sb, Te, from Goodfellow and S from Sigma-Aldrich. The required amounts of powders were mixed in an agate mortar during 15 minutes to obtain homogenous mixtures. The mixing and quartz ampoule filling steps were carried out in a nitrogen glove box. Then the QAs were vacuumed up to $5x10^{-5}$ mbar and sealed using a butane/oxygen torch. The sealed tubes were heated up vertically in a muffle furnace to 650°C within 12 hours then dwelled for 48 hours and slowly cooled down. The final products were ground and sieved through a mesh with a 150 µm opening. The powders were compacted in a graphite die by Spark Plasma Sintering (SPS) by heating up to 575°C with a heating rate of 100°C/min and keeping for a 15 min dwell under a pressure of 50 MPa. The pressure was released once the process was achieved at a temperature below 85°C. High density pellets with relative density >93% were achieved for all types of samples. This procedure led to samples which were composed of CoSbS as a majority phase. Some additional phases such as CoS_x, PdSb, and NiSb were found on samples doped with Pd and Ni respectively.

The Hall Effect measurements were carried out on an Ecopia 5AHT55T5 setup at room temperature (RT). The charge carriers concentrations (n) and mobility (ν) were measured on a Van der Pauw geometry on the linear part of I(V) curves. Electrical conductivity (σ) and Seebeck coefficient (S) were measured at room temperature by a Potential-Seebeck

Microprobe (Panco) and under a helium atmosphere from 340K to 730K on a LSR-3 (Linseis) setup. The thermal conductivity was calculated via $\kappa = D_f.c_p.d$, where D_f is the thermal diffusivity, c_p is the thermal capacity and d is the density. The thermal diffusivity was measured by the xenon flash method on a Netzsch LFA 467 under nitrogen flow and using Cape-Lehman fitting. The thermal capacity measurements were carried out on a DSC 404 with a Pt/Al_2O_3 crucible and a ramping rate of 5K/min. The electronic part of the thermal conductivity was calculated using the Wiedemann-Franz law with the Lorenz's number of $2.44x10^8$ W.Ω.K^{-2}. The X-ray diffraction patterns were collected on powders and pellets made by SPS. Scanning Electron Microscopy was carried out on a Hitachi S-4700 coupled with an Energy Dispersive X-rays Spectrometer.

The self-consistent DFT calculations for CoSbS were performed using the (L)APW+lo method[24] implemented within the WIEN2k code. A 7x7x3 k-mesh was used for the self-consistent DFT calculations. Subsequently, the bandstructure calculations were performed in a denser 18x17x9 k-mesh. All the DFT calculations were performed using the Perdew-Burke-Ernzerhof (PBE) or the Engel-Vosko (EV) exchange-correlation potential. The transport properties were evaluated using the BoltzTrap code.[25] Here, the Seebeck coefficient S and σ/τ are evaluated on an absolute scale. σ is the electrical conductivity and τ is the relaxation time. The defect calculations were performed in a 2x2x1 supercell using the VASP code with a 3x3x3 k-mesh. The energy of a particular defect D with charge q is [26,27],

$$E_d(D^q, \mu_e) = E_F(D^q) + q\mu_e - \sum_\alpha n_\alpha \Delta\mu_\alpha \qquad (1)$$

here $E_F(D^q) = E(D^q) - E_{bulk} - \sum_\alpha n_\alpha E_\alpha^{ref}$ is the formation energy of the defect D^q, with respect to its reference states. $E(D^q)$ is the energy of the supercell including the defect, E_{bulk} is the energy of pristine supercell; n_α and E_α^{ref} respectively are the number and energy of the reference states (α= Co, Sb, S and D). The defect energy $E_d(D^q, \mu_e)$ in Eq. (1) is additionally a
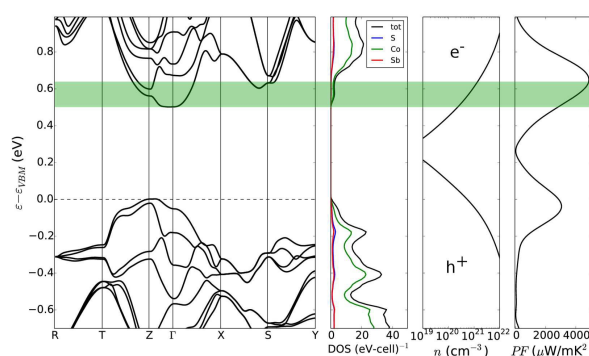
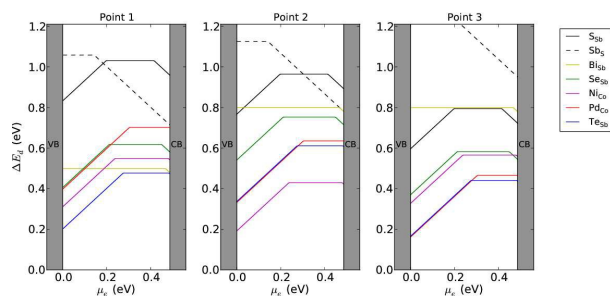**Fig. 1** The bandstructure, partial-Density of States (DOS), carrier concentration and PF of CoSbS evaluated from DFT. The shaded region represents an energy window of 150 meV, which approximately corresponds to the width of the derivative of the Fermi-function at 600 K. In the right panel τ=10^{-14} sec. The choice of τ is only to obtain an illustration of the dependence of the power factor on the electronic structure of CoSbS.

function of the electronic chemical potential, μ_e, i.e. $\Delta\mu_\alpha$ (α = Co, Sb, S, D), which are controlled by the competing phases, that in turn depend on the growth conditions. Thus, the elemental chemical potentials, $\Delta\mu_\alpha$ are variables; however their choices must eliminate the formation of competing phases and favour a thermodynamically stable CoSbS. Therefore our defect calculations in Figure 2 and Figure S2 will be presented at the edges of narrow triangular window of $\Delta\mu_\alpha$ illustrated in Figure 3. Figure S2 illustrates the defect formation energies for intrinsic defects. In particular $CoSb_3$, Co_9S_8 and Sb_2S_3 limit the $\Delta\mu_\alpha$ range (see Figure 3). These are roughly the same compensating phase compositions also observed by us when synthesizing CoSbS.
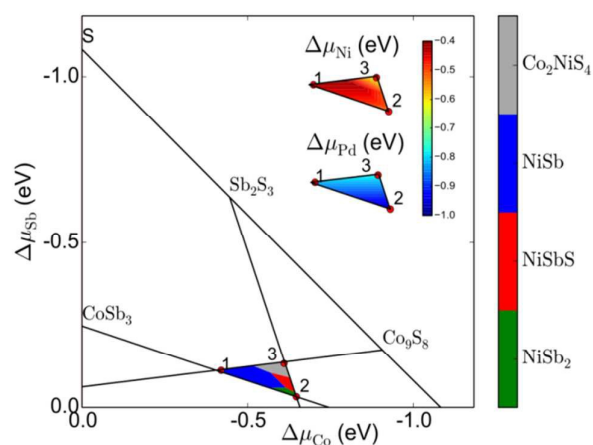
Results and discussion

The DFT bandstructure and the density of states (DOS) evaluated from DFT are revealed in Figure 1. We obtain that CoSbS is non-magnetic with an indirect bandgap of 0.5 eV. The CB edge predominantly has a Co 3d character. A collection of bands approximately 150 meV above the conduction band minimum (CBM) gives rise to a sharp increment in the DOS. We note that the width of the Femi distribution function at 600K would normally extend more than 150 meV into the CB in n-doped CoSbS. Figure 1 also illustrates that the two lowest conduction bands have several pockets in the orthorhombic Brillouin zone (BZ). Especially there are multiple electronic pockets around Z, Γ and S points. Such complex pocket shapes are known to result in favourable TE performances. Also illustrated in Figure 1 are the carrier concentration (n) and the computed PF as a function of energy in the band. We obtain a peak in the PF at approximately 150 meV within the CB. This is simultaneously accompanied by an increase in carrier concentration, in comparison to that at CBM edge. Hence, if one could potentially n-dope CoSbS such that the chemical potential μ_e is shifted upwards within the CB, the thermoelectric performance can be optimized. The amount of carriers that can be generated in a semiconductor depends on its detailed defect thermochemistry. First and foremost there should not be any compensating or killer intrinsic defects.

These defects will produce the opposite charged carrier as desired, thereby pinning the chemical potential in the middle of the gap and eventually leading to poor thermoelectric properties. For this reason we have calculated the energy of formation of intrinsic defects (vacancies, interstitial and anti-site defects) before searching for suitable extrinsic defects which may produce the desired charge carrier concentration. Defect formation energies of all intrinsic defects are shown in Figure S2 in the supplementary information. In Figure 2, we show only the dominating intrinsic defects, which are the anti-site defects S_{Sb} (S on the Sb position) and Sb_S. Due to the multivalent character of Sb, both defects can exist as positive and negative defects. As a result of the relatively high ΔE_d the calculated carrier concentration due to the intrinsic defects is approximately 10^{18} cm^{-3}. This will result in a high resistivity value and poor PF for the undoped sample. As seen in Table 1, this is in good agreement with the experimental results as we found that undoped CoSbS is n-doped with a carrier concentration around 5 10^{18} cm^{-3}. Furthermore, we note on Figure 2, that all the intrinsic defects are at least 0.5 eV in energy or higher, at the CBM. It is therefore possible to find purely electron doping (positively charged) extrinsic defects with a lower energy. In order to improve the carrier concentration and eventually the thermoelectric performance of CoSbS, we investigated the effect of doping with several potential candidates. A summary of all the extrinsic defect candidates investigated in this work is shown in Figure S3 and Table S1. In total we have investigated the effect of 49 extrinsic dopants. Our high-throughput DFT defect calculations reveal Ni, Pd and Te as promising dopant candidates for CoSbS. Apart from these, Bi and Se also show low defect energies.

Fig. 2 The dependence of the defect formation energies on the electronic chemical potential, μ_e, that spans within the bandgap of CoSbS is illustrated for stable extrinsic defects and the lowest energy intrinsic anti-site defect. ΔE_d vs μ_e is shown at three different values of elemental chemical potential, $\Delta\mu_\alpha$ with α = Co, Sb, S, corresponding to Fig 3 (see methods section for details). The high energy intrinsic defects are shown in detail in Figure S2.

Fig. 3 $\Delta\mu_\alpha$ values (α = Co, Sb, S) enclosed within the central triangle will result in thermodynamically stable CoSbS and exclude the formation of competing phases. The defect calculations are performed at points 1,2 and 3 which are at the extrema of the stable domain. The competing dopant phases in the case of Ni doping depend on $\Delta\mu_\alpha$ and are illustrated here. In the case of Pd doping, the dominating competing phase is $PdSb_2$, throughout the permitted region for $\Delta\mu_\alpha$ values. Additionally in the inset, the maximum allowed $\Delta\mu_D$ value that would prevent the formation of competing phases with the dopant D (Pd and Ni) is shown.

Table 1 Room temperature transport measurements carried out on CoSbS doped with effective dopants.

Dopant	Hall effect at RT		PSM at RT		
	n, cm^{-3}	v, cm^2.(V.s)$^{-1}$	ρ, mΩ.cm	S, μV.K^{-1}	PF, μW.m^{-1}.K^{-2}
undoped	- 4.75x10^{18}	5.3	293 ± 2.2	-459±36	72 ± 0.5
+2 at. % Bi	- 3.78x10^{18}	11.0	160 ± 8.2	-459±16	132 ± 7
+2 at. % Se	- 1.52x10^{19}	5.9	91 ± 0.4	-354±30	138 ± 0.5
+2 at. % Pd	- 7.7x10^{19}	9.7	10 ± 0.02	-185±8	342 ± 0.8
+2 at. % Ni	- 6.94x10^{19}	7.2	13 ± 0.1	-213±19	349 ± 2.4
+2 at. % Te	- 1.05x10^{20}	15.3	4.4 ± 0.02	-198±7	891 ± 4.2

The defect formation energies of D_{Co} with D = Ni, Pd and D_{Sb} with D = Bi, Se, Te are illustrated in Figure 2. Note that the three points for which the defect energies are reported in Figure 2, correspond to the edges of the allowed chemical potential values that would produce a thermodynamically stable CoSbS host.

In general, we observe that Ni_{Co}, Te_{Sb} and Pd_{Co} are the defects with the lowest energies for all the three points and they will not be affected by any intrinsic defects. Each of the three short-listed extrinsic defects are positively charged (q=+1) and thus will generate electrons into the conduction bands. This is somewhat intuitive, since Ni and Pd have an extra valence electron than Co, and the same is true for Se and Te with respect to Sb. As expected, the defect formation energies of the Pd_{Co} and Ni_{Co} defects are higher at the Cobalt rich point 1 (low $|\Delta\mu_{Co}|$) than at point 2. The Te_{Sb} defect is highest in energy at point 2 as this is the Sb richest (lowest $|\Delta\mu_{Sb}|$) point. Interestingly the Pd_{Co} is stabilized at point 3, whereas the Ni_{Co} is destabilized. The stabilization of Pd_{Co} can be explained by point 3 being Sb poorer (higher $|\Delta\mu_{Sb}|$) than point 2. Thereby the Sb-rich phase, $PdSb_2$, which is the dominant competing phase in the entire region in case of Pd doping, is restricted. This effect is not observed for Ni_{Co} because point 3 is also Sulfur richer than point 2, whereby a number of Ni-S phases become limiting phases. As illustrated in Figure 3, the dominating competing phase at point 3 is the Co_2NiS_4 phase. Even in the absence of this phase, a number of Ni-S phases, e.g. Ni_3S_4, set a stricter limit on $|\Delta\mu_{Ni}|$ than $NiSb_2$. Our theoretical defect calculations indicate that Pd and Te could be effective n-dopants in CoSbS in addition to Ni. In
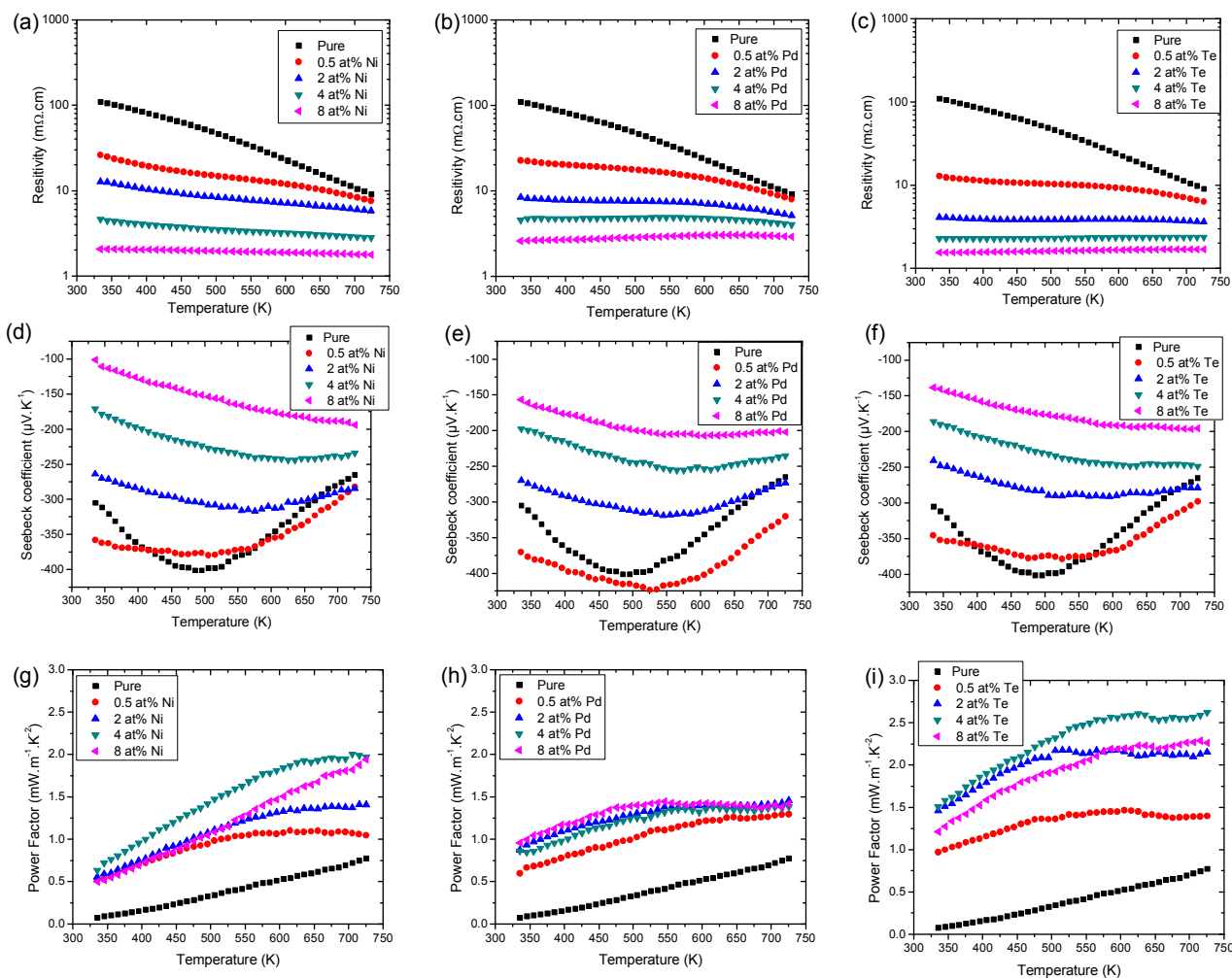
Fig. 4 Temperature dependent Seebeck coefficient, electrical resistivity and power factor for Te, Ni and Pd doped CoSbS. The presented data are average values of 6 measurements, a variation of +/- 10% is observed on the PF values.

particular Te and Pd as dopants are favored at different growth conditions (except Sb rich), and are not influenced drastically by their dopant competing phases compared to Ni which exhibits a very rich Ni-S chemistry. Figure 1d illustrates the calculated electron chemical potentials that can be achieved by Ni and Te doping in the sulfur rich (point 3) limit, and underlines that a substantial improvement in power factor should be attainable over the previous results obtained with Ni-doping.[22,23]

The experimental transport measurements at T=300 K and 2 at./mol. % of the effective dopant α, are reported in Table 1. In particular we summarize, the carrier concentration and mobility evaluated from Hall effect, the resistivity, the Seebeck coefficient and the PF measured with the PSM setup. Compared to the undoped sample, we observe a pronounced improvement of the thermoelectric performance in n-doped CoSbS. In the Ni and Pd-doped samples a fivefold increase in PF is achieved and in the Te-doped the PF is increased by a factor of 12. This corroborates the low defect formation energies of Ni_{Co} Pd_{Co} and Te_{Sb} defects. Moreover, the results summarized in Table 1 indicate that the drop of the resistivity occurs not only because the charge carrier concentration increases but also because the mobility of charge carrier increases. It is clear that among all tested elements, Te, Pd and Ni are the most promising dopants for CoSbS. The results (Table S2) and discussions of the non-effective dopants are discussed in the supplementary information section.

Note that in Table 1 the PF at room temperature in the case of Te doped CoSbS is about 0.5 $mW.m^{-1}.K^{-2}$ higher than that for Ni and Pd doped CoSbS. Clearly such a high PF value indicates that an important experimental work of dopant optimization is necessary, especially in the case of Te doped CoSbS. Furthermore, we observe a high mobility of 15.3 $cm^2/V.s$ for Te doped samples. Table 1 does indicate an increased mobility with increasing carrier concentration. This is in accordance with the increased population of the multiple pockets approximately 150 meV above the conduction band edge. From the PSM measurements, an increase of the power factor in comparison to the undoped sample has been observed when CoSbS is n-doped with Bi, Se, Pd and Te. In the cases of Bi and Se doping, we observe that the PF is doubled in contrast to that of undoped CoSbS. However, in the case of Bi doping the Hall carrier concentration is still low, i.e. 3.8 x 10^{18} electrons per cm^3. This is supported by our defect calculations in Figure 2, which illustrates that the lowest BiSb defect is uncharged (Bi and Sb are isoelectronic) and furthermore higher in energy (750 meV). The large increase in PF for Bi doped CoSbS is explained due to a relatively high mobility of μ=11.0 $cm^2/V.s$, which is two-fold increased with respect to the undoped sample. For Se-doped CoSbS the Hall carrier concentration is slightly more than double the magnitude for the undoped case. This agrees with the observation of a lower energy electron producing Se_{Sb} defect. Consequently, we obtain a decrease of the resistivity by a factor of 3 and a slight

decrease of the absolute Seebeck coefficient, which collectively results in an improved PF. Based on these results, three series of samples have been prepared to study in more details the effect of Sb site substitution in CoSbS by Te, and Co site substitution by Ni and Pd.

The summary of electrical resistivity and Seebeck coefficient measurements versus temperature for CoSbS doped with Nickel, Palladium and Tellurium is presented on Figure 4. The presented results are an average value of 6 measurements in a temperature range from 340K to 730K. The undoped as well as the 0.5 at. % and 2 at. % doped CoSbS show a U-shaped temperature dependence of the Seebeck coefficient versus temperature characteristic of a semiconducting thermoelectric material. In heavily doped samples with 4 and 8 at. % of doping element, the absolute Seebeck coefficient increases with temperature, while in parallel, the electrical resistivity tends to decrease. This behaviour is rather unusual for a thermoelectric material. However, a similar trend has been observed in half-Heusler[28-30] compounds. It could tentatively be attributed to a shift from a defect dominated scattering regime to an acoustic phonon dominated regime as the electron concentration is increased above 10^{20} cm^{-3} (e.g. 2.7x10^{20} and 5.8x10^{20} cm^{-3} for 4 at. % and 8 at. % of Te, respectively). Moreover, the comparison of charge carrier mobility at different doping concentrations indicates that it may increase with charge carrier concentration which is quite interesting. Indeed, the charge carrier mobility measured at room temperature on polycrystalline samples with 4 at. % and 8 at. % dopant increased from 15 to 21 $cm^2/V.s$ for Palladium doping and from 7.6 to 33.5 $cm^2/V.s$ for Nickel doping, respectively. Strong variations of the thermoelectric properties may indicate that the electronic band structure is modified by dopants or temperature. Moreover, modifications of the electronic band structures may lead to the formation of resonant states[31] or to electronic bands convergence.[32]

Furthermore, we have observed that the doping with Te and Pd increases the unit cell volume (Figure S8). This modification of the lattice parameters could also alter the electronic band structure. As one can see in Figure 1, the electronic pockets around the S point is about 150 meV from the CBM, which is constituted around the Γ point. We suspect that the increase of the dopant concentration as well as the increase of temperature allows the electronic pocket around the S point to additionally contribute to the electron transport. Detailed discussion on the volume dependent changes in the bandstructure of CoSbS, is beyond the scope of the present paper but will be discussed in an accompanying publication. It is worth mentioning here though that we have performed temperature dependent Hall Effect measurements in order to further investigate this peculiar behaviour. However, so far, these measurements failed for some unclear reasons mainly due to large noise appearing with increasing temperature.
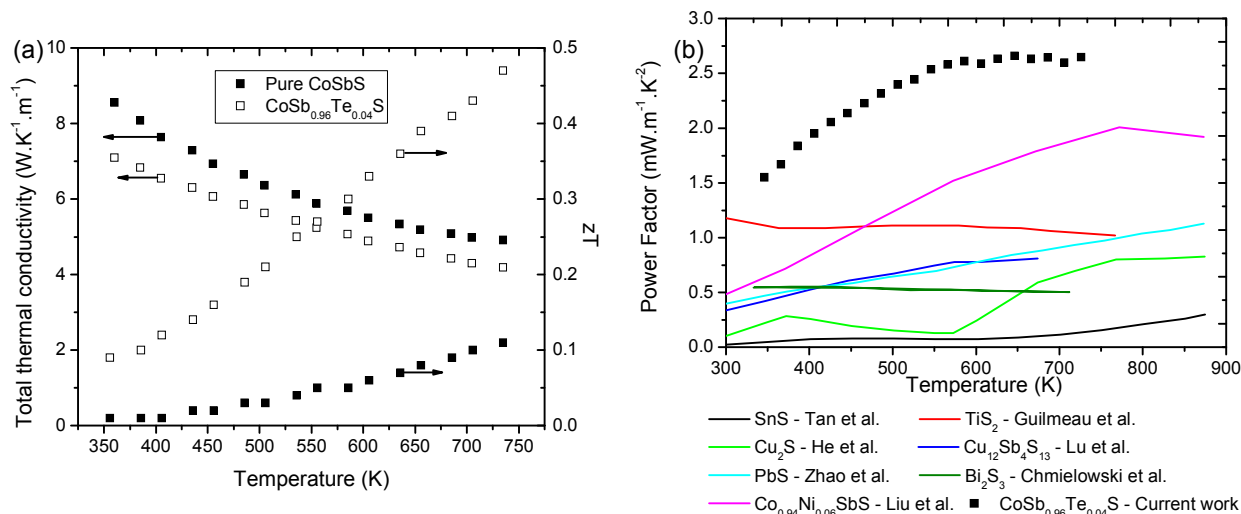
Fig. 5 (a) Total thermal conductivity and zT of pure and doped CoSbS, (b) Power factor of CoSb$_{0.96}$Te$_{0.04}$S in comparison with other high performing sulfur based thermoelectric materials.

Nevertheless, whatever the reasons of these unconventional behaviours are, they are leading to an important increase of the power factor. For Tellurium doping the CoSbS power factor rises from 0.07 to 1.5 mW.m^{-1}.K^{-2} and from 0.77 to 2.7 mW.m^{-1}.K^{-2} at 330K and 725K, respectively. For the Palladium and Nickel doping lower increases of PF are observed. The maximum power factor for Palladium and Nickel doping are 1.5 mW.m^{-1}.K^{-2} and 2.0 mW.m^{-1}.K^{-2}, respectively. Based on these results we concluded that the highest power factor is observed on samples with a dopant concentration around 4 at. %. In the case of Palladium, a plateau of power factor is observed from 2 to 8 at. % of Palladium. We believe that this plateau might be due to the appearance of a PdSb phase. The increase of the PdSb content with the increase of the Palladium concentration has been observed on XRD patterns collected on Pd series (Figure S4). The inclusion of PdSb phase was also observed by SEM/EDX (Figure S5). We suspect that the solubility of Pd in CoSbS is limited thus Palladium is less efficient than Ni and Te.

As a last comment, we believe that in the case of doping by substitution of Sb, the system benefits from a synergistic effect related to a reduction of compensating defects. Indeed, as indicated by the calculations of the energy formation of intrinsic point defects shown in Figure S2, the only competing intrinsic p-type defect is Sb$_S$: This latter has a relatively low energy formation with ΔE_d below 1 eV. While doping with Te, we have observed that the conductivity achieved was higher in the cases where we removed as much Sb as we added Te. In other words, CoSb$_{0.96}$Te$_{0.04}$S showed better performances than CoSbTe$_{0.04}$. We think that this effect is related to the lower amount of compensating Sb$_S$ defect present.

As a summary a benchmark of the power factor of CoSb$_{0.96}$Te$_{0.04}$S in comparison to other high performing sulfur based thermoelectric materials is presented in Figure 5b. As one can see such high power factor values have never been reported for Sulfur based polycrystalline thermoelectric materials. Besides, to obtain an evaluation of the zT value for this new material we have performed thermal conductivity measurements. Figure 5a shows the total thermal conductivity and zT measured on an undoped and 4 at. % Te doped CoSbS. The thermal capacity and thermal diffusivity are presented in supporting information part (Figure S6). The total thermal conductivity is relatively high but decreases from 10 to 8 W.m^{-1}.K^{-1} at 330K when CoSbS is alloyed with Tellurium. This decrease of the total thermal conductivity goes with a significant decrease of the electrical resistivity (by a factor of 45). This indicates that the total thermal conductivity is driven by the lattice part rather than by the electronic part of the thermal conductivity. This observation is in good agreement with the estimation of the electronic part based on the Wiedemann-Franz law. Considering CoSbS doped with 4 at. % of Tellurium as a degenerated semiconductor we found that the electronic part of the total thermal conductivity is low and does not exceed 5 and 15% of the total thermal conductivity at 330K and 725K, respectively. Finally, the slight reduction of the thermal conductivity as well as the enhancement of the power factor caused by the Tellurium doping lead to a significant increase of the figure of merit. A zT of 0.47 at 725K has been observed.

Conclusions

A detailed study on the CoSbS dopability has been presented describing the screening for best performing CoSbS dopants. By computationally screening of potential dopants, we shortlisted Ni, Pd and Te as the most promising ones. We have demonstrated that these dopants may significantly increase the charge carrier concentration and thus enhance the thermoelectric properties of CoSbS. For Tellurium alloying we

have observed a power factor which exceeds 2.7 mW.m^{-1}.K^{-2} at 543 K, thereby out-performing significantly Ni alloyed CoSbS. To the best of our knowledge, such high value has never been reported for a polycrystalline semiconducting sulfur based material. Without any attempts of a reduction of thermal conductivity (e.g. through nanostructuring) this material presents already a zT of 0.47 at 725K. However, as we have observed that the total thermal conductivity of CoSbS is largely driven by the lattice part we believe that a significant decrease of the thermal conductivity introduced by points defects or nanostructures[33,34] may lead to a zT above 1. Thus, the presented results open a large variety of investigations such as complex nanostructuring or alloying. Moreover, as the observed temperature behavior of CoSbS remains unusual for a thermoelectric material to clarify these observations deeper theoretical studies are also welcome. All these new findings make CoSbS a new exciting thermoelectric material.

Author contributions

G.D. and R.C. conceived and led the project. R.C. supervised the experimental parts. S.B., R.S. and G.M. performed the DFT calculations. D.P., S.J. and K.M. carried out preparations and characterizations of samples with various dopants. W.X. and A.W. performed the DSC measurements. G.D., R.C., S.B. and G.M. wrote the manuscript, with feedback from all co-authors.

References

1   C. B. Vining, *Nature Materials*, 2009, **8**, 83.
2   A. J. Minnich, M. S. Dresselhaus, Z. F. Ren and G. Chen, *Energy Environ. Sci.*, 2009, **2**, 466.
3   M. W. Gaultois, T. D. Sparks, C. K. H. Borg, R. Seshadri, W. D. Bonificio and D. R. Clarke, *Chem. Mater.,* 2013, **25**, 2911.
4   Y. He, T. Day, T. Zhang, H. Liu, X. Shi, L. Chen and G. J. Snyder, *Adv. Mater.*, 2014, **26**, 3974.
5   C. Bera, S. Jacob, I. Opahle, N. S. H. Gunda , R. Chmielowski, G. Dennler and G. K. H.Madsen, *Phys. Chem. Chem. Phys.*, 2014, **16**, 19894.
6   K. Suekuni, K. Tsuruta, T. Ariga and M. Koyano, *Appl. Phys. Exp.*, 2012, **5**, 051201.
7   X. Lu, D. T. Morelli, Y. Xia, F. Zhou, V. Ozolins, H. Chi, X. Zhou and C. Uher, *Adv. Energy Mater.*, 2013, **3**, 342.
8   J. Heo, G. Laurita, S. Muir, M. A. Subramanian and D. A. Keszler, *Chem. Mater.*, 2014, **26**, 2047.
9   L. D. Zhao, S. H. Lo, J. Q. He, H. Li, K. Biswas, J. Androulakis, C. I. Wu, T. P. Hogan, D. Y. Chung, V. P. Dravid and M. G. Kanatzidis, *J. Am. Chem. Soc.*, 2011, **133**, 20476.
10 L. D. Zhao, J. He, C. I. Wu, T. P. Hogan, X. Zhou, C. Uher, V. P. Dravid and M. G. Kanatzidis, *J. Am. Chem. Soc.*, 2012, **134**, 7902.
11 L. D. Zhao, J. He, S. Hao, C. I. Wu, T. P. Hogan, C. Wolverton, V. P. Dravid and M. G. Kanatzidis, *J. Am. Chem. Soc.*, 2012, **134**, 16327.
12 Z. H. Ge, B. P. Zhang, Y. X. Chen, Z. X. Yu, Y. Liu and J. F. Li, *Chem. Commun.*, 2011, **47**, 12697.
13 Q. Tan, L. D. Zhao, J. F. Li, C. F. Wu, T. R. Wei, Z. B. Xing and M. G. Kanatzidis, *J. Mater. Chem. A*, 2014, **2**, 17302.
14 J. Corps, P. Vaqueiro and A. V. Powell, *J. Mater. Chem. A*, 2013, **1**, 6553.
15 E. Guilmeau, Y. Bréard and A. Maignan, *Appl. Phys. Lett.*, 2011, **99**, 052107.
16 K. Biswas, L. D. Zhao and M. G. Kanatzidis, *Adv. Energy Mater.*, 2012, **2**, 634.
17 R. Chmielowski, D. Péré, C. Bera, I. Opahle, W. Xie, S. Jacob, F. Capet, P. Roussel, A. Weidenkaff, G. K. H. Madsen and G. Dennler, *J. Appl. Phys.*, 2015, **117**, 125103.
18 G. Dennler, R. Chmielowski, S. Jacob, F. Capet, P. Roussel, S. Zastrow, K. Nielsch, I. Opahle, and Madsen G. K. H., *Adv. Energy Mater.*, 2014, **4**, 1301581.
19 L. J. Cabri, D. C. Harris and J. M. Stewart, *Canadian Mineralogist*, 1970, **10**, 232.
20 F. Hulliger, *Helvetica Physica Acta*, 1959, **32**, 615.
21 R. Carlini, C. Artini, G. Borzone, R. Masini, G. Zanicchi and G. A. Costa, *J. Therm. Anal. Calorim.*, 2011, **103**, 23.
22 D. Parker, A. F. May, H. Wang, M. A. McGuire, B. C. Sales and D. J. Singh, *Phy. Rev. B.*, 2013, **87**, 045205.
23 Z. Liu, H. Geng, J. Shuai, Z. Wang, J. Mao, D. Wang, Q. Jie, W. Cai, J. Sui and Z. Ren, *J. Mater. Chem. C*, 2015, **3**, 10442.
24 G. K. H. Madsen, P. Blaha, K. Schwarz, E. Sjöstedt and L. Nordstroem, *Phys. Rev. B*, 2001, **64**, 195134.
25 G. K. H. Madsen and D. J. Singh, Comput. Phys. Commun. 2006, **175**, 67.
26 C. G. Van de Walle and J. Neugebauer, *J. Appl. Phys.*, 2004, **95**, 3851.
27 S. Bhattacharya, N. S. H. Gunda, R. Stern, S. Jacobs, R. Chmielowski, G. Dennler and G. K. H. Madsen, *Phys. Chem. Chem. Phys.*, 2015, **17**, 9161.
28 H. Xie, H. Wang, C. Fu, Y. Liu, G. J. Snyder, X. Zhao and T. Zhu, *Sci. Rep.* 2014, **4**, 6888.
29 S. Sakurada and N. Shutoh, Appl. Phys. Lett., 2005, **86**, 082105.
30 H. Xie, H. Wang, Y. Pei, C. Fu, X. Liu, G. J. Snyder, X. Zhao and T. Zhu, *Adv. Funct. Mater.*, 2013, **23**, 5123.
31 J. P. Heremans, B. Wiendlocha and A. M. Chamoire, *Energy Environ. Sci.*, 2012, **5**, 5510.
32 Y. Pei, A. LaLonde, H. Wang, L. Chen and G. J. Snyder, *Nature*, 2011, **473**, 66.
33 K. Biswas, J. He, I. D. Blum, C. I. Wu, T. P. Hogan, D. N. Seidman, V. P. Dravid and M. G. Kanatzidis, *Nature*, 2012, **486**, 414.
34 Y. Lan, A. J. Minnich, G. Chen and Z. Ren, *Adv. Funct. Mater.*, 2010, **20**, 357.